

Vortex pinning and dynamics in the neutron star crust

Gabriel Wlazłowski,^{1,2,*} Kazuyuki Sekizawa,^{1,†} Piotr Magierski,^{1,2,‡} Aurel Bulgac,^{2,§} and Michael McNeil Forbes^{3,2,¶}

¹*Faculty of Physics, Warsaw University of Technology,
Ulica Koszykowa 75, 00-662 Warsaw, POLAND*

²*Department of Physics, University of Washington, Seattle, Washington 98195-1560, USA*

³*Department of Physics & Astronomy, Washington State University, Pullman, WA 98164-2814, USA*

(Dated: October 17, 2018)

The nature of the interaction between superfluid vortices and the neutron star crust, conjectured by Anderson and Itoh in 1975 to be at the heart vortex creep and the cause of glitches, has been a long-standing question in astrophysics. Using a qualitatively new approach, we follow the dynamics as superfluid vortices move in response to the presence of “nuclei” (nuclear defects in the crust). The resulting motion is perpendicular to the force, similar to the motion of a spinning top when pushed. We show that nuclei repel vortices in the neutron star crust, and characterize the force as a function of the vortex-nucleus separation.

PACS numbers: 26.60.Gj, 03.75.Kk, 67.10.Jn, 67.25.dk

Introduction Pulsar glitches, sudden increases in the pulsation frequency first observed in 1969 [1, 2], provide one of the few observable probes into the interior of neutron stars [3]. Although many models have been proposed, the origin of large glitches remains a mystery. The current picture, proposed in 1975 by Anderson and Itoh [4], is that the quantized vortices in the superfluid interior of a neutron star store a significant amount of angular momentum. As these vortices “creep” through the crust, they transfer this angular momentum to the crust. Glitches result from a catastrophic release of pinned vorticity [5] that suddenly changes the pulsation rate.

This scenario involves two critical ingredients: the trigger mechanism for the catastrophic release (not considered here) and the vortex-“nucleus” interaction. (By “nucleus” we mean nucleilike objects embedded in a neutron superfluid as is expected in the crust of neutron stars.) The interaction can, in principle, be derived from a microscopic theory. However, despite considerable theoretical effort, even its sign remains uncertain. Until now, the force was evaluated by comparing (free) energies extracted from different static calculations: a vortex passing through a nucleus, a vortex and nucleus separated by an infinite distance, or an interstitial vortex between two neighboring nuclei [6–12]. As pointed out in Ref. [13], this approach only computes the pinning energy, and is not able to extract the full information about the vortex-nucleus interaction.

Despite these efforts, there is still no agreement about whether pinned or unpinned configurations are preferred. The problem is that subtracting two large energies arising from many contributions, typically of order 10^4 MeV, results in a tiny difference of order 1 MeV. Symmetry-unrestricted calculations are challenging, and only by imposing axial symmetry has the required 1 MeV accuracy been achieved [12, 14]. Moreover, the difference is ex-

tremely sensitive to quantum shell effects that are not present in semiclassical simulations [6–9], and is sensitive to the particle number or background density which varies from one configuration to the next. (See [12] for extensive discussion.)

Here we show that nuclei repel superfluid vortices and characterize the vortex-nucleus interaction within dynamical simulations as suggested in [15]. The sign of the force can be unambiguously determined by looking at the vortex motion (see the movie demonstrating the response of classical gyroscope when pushed in the Supplemental Material [16]). In 3D dynamical simulations, all relevant degrees of freedom of the vortex-nucleus system are active, and the behavior provides valuable insight for building effective theories of the vortex-nucleus system. Following [17], an effective hydrodynamic description can be formulated (see also [18–21])

$$T \frac{\partial^2 \mathbf{r}}{\partial z^2} + \rho_s \boldsymbol{\kappa} \times \left(\frac{\partial \mathbf{r}}{\partial t} - \mathbf{v}_s \right) + \mathbf{f}_{\text{VN}} = 0, \quad (1)$$

where \mathbf{r} is the position of the vortex core. The first term is tension force as the vortex is bent, characterized by coefficient T . The second term corresponds to Magnus force where $\boldsymbol{\kappa} = 2\pi\hbar\hat{\mathbf{l}}/2m_n$ is the circulation which points along the vortex, $\rho_s = m_n n$ is mass density while n is number density of superfluid neutron background, m_n is neutron mass, and \mathbf{v}_s is the velocity of any ambient flow in the background superfluid density. The last contribution \mathbf{f}_{VN} defines the vortex-nucleus interaction in terms of the force per unit length. Clearly the pinning energy alone does not provide sufficient information to describe the motion. In addition, all existing calculations assume that the vortices form straight lines, and thus do not reveal information about the tension. It is demonstrated in [17] that pinning occurs irrespective of the sign of the vortex-nucleus interaction when

$v_s < v_c \sim s^{1/2} F_m / \rho_s \kappa a$, where F_m is set by maximum magnitude of \mathbf{f}_{VN} , $s = F_m / T$, and a is set by range of vortex-nucleus interaction. In this work we extract all effective quantities directly from a microscopic theory.

Method The most accurate and flexible microscopic approach to superfluid dynamics in nuclear systems is density functional theory (DFT), which in principle is an exact approach. Here we use an extension of Kohn-Sham DFT known as the time-dependent superfluid local density approximation (TDSLDA), an orbital-based fermionic DFT that has been proven to be very accurate for describing the dynamics of strongly correlated fermionic systems in both ultracold atomic gases [22–28] and in nuclear systems [29–32]. In this approach, densities and the superfluid order parameter Δ are constructed from quasiparticle orbitals which are represented on a 3D lattice (without any symmetry restrictions) of size $75 \text{ fm} \times 75 \text{ fm} \times 60 \text{ fm}$ with lattice spacing corresponding to quite a large momentum cutoff $p_c \approx 400 \text{ MeV}/c$, and a volume that is sufficient to fit a single nucleus and a quantum vortex with reasonable separation between the two. To prevent vortices from neighboring cells from interacting (due to the periodic boundary conditions), we introduce a flat-bottomed external potential confining the system in a tube of a radius 30 fm . (See [16] and [14] for details.) For initial states in our time-dependent simulations we chose stationary self-consistent solutions of the TDSLDA with two constraints: i) the center of mass of the protons is fixed at a specified position, ii) the phase of the neutron pairing potential increases by 2π when moving around the center of the tube, i.e. $\Delta(\rho, z, \phi) = |\Delta(\rho, z)| \exp(i\phi)$, where $\rho = \sqrt{x^2 + y^2}$ is the distance from the center of the tube and $\phi = \tan^{-1} \frac{y}{x}$. We produce initial states for two background neutron densities, $n = 0.014 \text{ fm}^{-3}$ and $n = 0.031 \text{ fm}^{-3}$, with proton number $Z = 50$. These represent the zones 3 and 4 expected in neutron star crusts according to the classification of Negele and Vautherin [33]. Previous calculations are in clear disagreement in this region of densities. We start the simulations from two configurations: an *unpinned* configuration where the nucleus is located outside the vortex, close to the tube boundary, and a *pinned* configuration where the nucleus is located inside the vortex (see [16] for figures of these states).

The physics contained in the DFT is defined by the energy density functional \mathcal{E} which is a functional of the single-particle orbitals. For the normal part we use the FaNDF⁰ functional constructed by Fayans et al. [34, 35]. It reproduces the infinite matter equation of state of Refs. [36, 37], many properties of nuclei [38, 39], and allows one to construct a very efficient solver of the TDSLDA equations (see [16]). The only simplification we make is to omit the spin-orbit coupling term from the functional as this greatly reduces the computational cost. While the spin-orbit term is important for finite nuclei, in the present context it is not expected to significantly

impact the final results. The spin-orbit term does not affect uniform matter, thus in our case where the “nuclei” are embedded in a uniform gas of neutrons, it would shift the single-particle levels in the “nucleus” in such a way as not to influence the physics of the vortex-nucleus system, as shown in [12]. These hardly influence the physics of the vortex-nucleus system. Likewise, since the depletion of the normal density in the vortex core is small [40], the vortex density is approximately uniform and one expects the influence of the spin-orbit term on the structure of the vortex to be small. To the FaNDF⁰ functional we add a contribution describing the pairing correlations, $\mathcal{E}_{\text{pair}}(\mathbf{r}) = g(n(\mathbf{r}))|\nu_n(\mathbf{r})|^2 + g(p(\mathbf{r}))|\nu_p(\mathbf{r})|^2$, where $\nu_{p,n}$ are the $S = 0$ proton and neutron anomalous densities (proportional to the superfluid order parameter and pairing gaps $\Delta_{n,p}$), g is a density dependent coupling constant, and n/p is density of neutrons/protons. The coupling constant g is chosen so as to reproduce the neutron pairing gap in pure neutron matter. It has the density dependence as predicted by BCS, but with maximum pairing gap of 2 MeV (the full form is shown in [16]). The local portion of the anomalous densities $\nu_{n,p}$ diverges and requires regularization. We use the procedure described in Refs [41, 42], the accuracy of which has been validated against a wide range of experimental results for cold atoms [22, 23, 25–28, 43–45] and nuclear problems [29, 31, 38, 40].

The TDSLDA approach automatically includes various dissipative processes, including superfluid and normal phonon excitations, Cooper pair breaking, and Landau damping. These are crucial for a correct description of vortex pinning and unpinning [46]. Consider pinning: for a nucleus to capture a vortex, the vortex must dissipate its collective energy, otherwise it will simply orbit the nucleus as governed by the Magnus force, like a precessing spinning top. We demonstrated in [28] that the TDSLDA accurately models the formation and decay of solitonic defects – from domain walls into vortex rings and vortex lines. These effects cannot be reproduced without dissipation, and the agreement with experiments [47, 48] validates that the so-called one-body dissipation naturally present in the TDSLDA is sufficient to correctly capture vortex dynamics. With the TDSLDA approach, we can thus extract both the magnitude of the vortex-nucleus interaction as well as the dynamical time scales.

To extract the effective force between a quantized vortex and a nucleus, we apply Newton’s laws. Suppose that only two forces act on the nucleus: the force \mathbf{F} arising from the interaction with the vortex and a known external force \mathbf{F}_{ext} . In the simplest case, the vortex-nucleus force depends on the relative distance between interacting objects R . If the nucleus moves with a constant velocity \mathbf{v}_0 which is below the critical velocity (so that phonons are not excited), then the relation $\mathbf{F}(t) = -\mathbf{F}_{\text{ext}}(t)$ holds. Combining this information with the relative distance $R(t)$ we can extract the vortex-nucleus force as a function

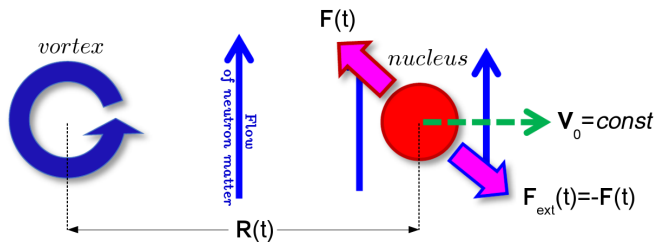


FIG. 1. (Color online) Schematic figure explaining the method used for the force extraction. The force \mathbf{F} depends on relative distance between vortex and nucleus R , moving with a constant velocity \mathbf{v}_0 . The external force $\mathbf{F}_{\text{ext}}(t)$ is chosen to compensate exactly \mathbf{F} .

of the separation $\mathbf{F}(R)$, see Fig. 1. We choose the external force to be constant in space and acting only on the protons. This force moves the center of mass of the protons together with those neutrons bound (entrained) in the nucleus without significantly modifying the internal structure of the nucleus or surrounding neutron medium. We adjust the force to ensure that the center of mass of the protons moves with constant velocity \mathbf{v}_0 :

$$\mathbf{F}_{\text{ext}}(t + \Delta t) = \mathbf{F}_{\text{ext}}(t) - \alpha [\mathbf{v}(t) - \mathbf{v}_0], \quad (2)$$

where $\mathbf{v}(t)$ is the velocity of the center of mass of protons and α is the coefficient governing the rate of adjusting the force. In our simulations we dragged the nucleus with a very small velocity $v_0 = 0.001c$ along the x axis to ensure that no phonons are excited. The velocity is far below the critical velocity of the system and is sufficiently small that the systems follow an almost adiabatic path.

Results of dynamical simulations In the first set of simulations, we start from an unpinned configuration and drag the nucleus towards the vortex. Fig. 2 shows the time evolution of these systems for small vortex-nucleus separations (see [16] for movies of the entire simulations). As the nucleus approaches to the vortex, it exerts a force $\mathbf{F}(R)$ on the vortex which responds by moving according to the Magnus relationship $\mathbf{F}_M \propto \boldsymbol{\kappa} \times \frac{\partial \mathbf{r}}{\partial t}$, where \mathbf{r} specifies the vortex-core position. The vortex is initially moving perpendicular to this force along positive y direction visually confirming that the force is indeed repulsive and initially directed along the x axis away from the nucleus. In the case of attraction the vortex would initially move along the negative y direction. For both densities considered, the vortex-nucleus interaction is clearly repulsive and increasing with density, a result in agreement with the hydrodynamic approximation [16]. The curvature of the vortex bending for the closest vortex-nucleus configuration is set by the nucleus. (There is also a small displacement of both ends of the vortex during the evolution in our simulation box.) For the higher density, the vortex induces visible nuclear prolate deformation with the elongation axis set by the vortex axis. To confirm the repulsive nature of the force at very small vortex-nucleus

separations, we also start simulations from “pinned” configurations. In both cases the vortex rapidly unpins (with a timescale shorter than 1,000 fm/c), i.e., the vortex is immediately expelled from the nucleus, indicating that the pinned configuration is dynamically unstable. The initial energy is transferred into stretching of the vortex line as it bows out away from the nucleus.

We will proceed now to estimate the vortex tension T . The vortex is the longest at $t_{\text{max}} \approx 14,000$ fm/c for both low and high densities, 0.014 fm^{-3} and 0.031 fm^{-3} respectively. The length of the vortex increases by $\Delta L = L(t_{\text{max}}) - L(0) = 3.5$ fm and 1.5 fm and the total excitation energy of the system is $E^* = E(t_{\text{max}}) - E(0) = 5$ MeV and 11 MeV respectively. Assuming all of this energy is stored in the vortex, we obtain an upper bound on the vortex tension of $T \lesssim 1.4$ MeV/fm and 7.3 MeV/fm, respectively. The energy of a vortex line in the leading order hydrodynamic approximation is $E \approx \rho_s \kappa^2 L \ln(D/2\xi)/4\pi$ [16], where D is the diameter of the simulation cell, which has to be replaced with the average vortex separation l_v in the neutron star crust [49]. This simple hydrodynamic approximation suggests that different tensions arise from changes in the neutron superfluid density ρ_s and vortex core size ξ . Estimating $\rho_s \sim n$ gives a ratio of 0.77 [10], which is much larger than the ratio $1.4/7.3 \approx 0.18$ obtained from our microscopic simulations. At higher densities the vortex is thus much stiffer than expected from hydrodynamic estimates.

Force per unit vortex length Combining the information about the force $\mathbf{F}(t)$ with the vortex-nucleus separation $R(t)$, we extract the force for various separations R , defined as the distance within the plane perpendicular to the symmetry axis of the confining tube. We decompose the force into a tangential and a centripetal components with respect to the vortex position at each time. These results are presented in the inset (b) of Fig. 3. The extracted force is predominantly central with a negligible tangential component. The effective range of the force is about 10 fm for the lower density, increasing to about 15 fm for the higher density, consistent with an increasing coherence length ξ with density and decreasing neutron pairing gap. The behavior of the total force for small separations demonstrates that it is not merely a function of a distance. At small separations, the deformation of the vortex line and the nuclear deformation become important degrees of freedom.

To characterize the effects of the vortex geometry, we extract the force per unit length $f(r)$. Inspired by the vortex filament model (see [50, 51] and references therein), we divide the vortex line into elements of length $d\mathbf{l}$. Each element exerts force on a nucleus

$$d\mathbf{F} = f(r) \sin \alpha \hat{\mathbf{r}} d\mathbf{l}, \quad (3)$$

where \mathbf{r} denotes the position of the vortex line element from the center of mass of the protons, α is angle between vectors $d\mathbf{l}$ and \mathbf{r} (see inset (a) of Fig. 3), and $\hat{\mathbf{r}} = \mathbf{r}/r$.

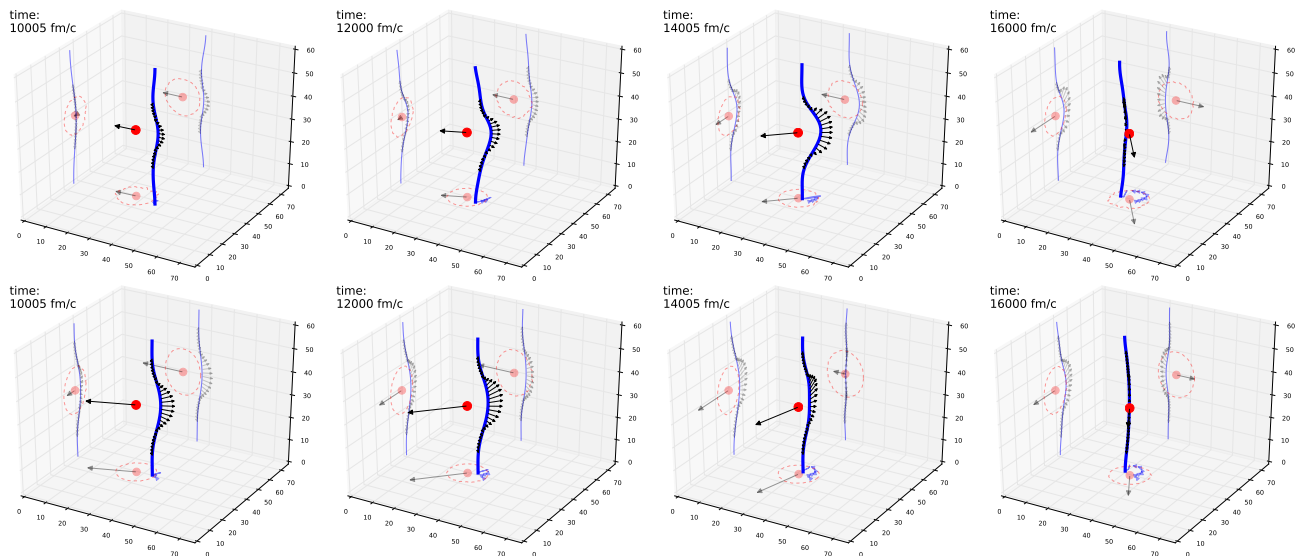


FIG. 2. (Color online) Dynamics of the system for times corresponding to small vortex-nucleus separations for neutron matter density $n = 0.014 \text{ fm}^{-3}$ (top) and 0.031 fm^{-3} (bottom). Frames from left to right correspond to times $(10, 12, 14, 16) \times 1,000 \text{ fm}/c$ (for full movies see [16]). Blue line indicates the vortex core position extracted from the order parameter Δ (see [16] for details). Red dot indicates position of the center of mass of protons. The vector attached to the red dot denotes the vortex-nucleus force $\mathbf{F}(R)$. Vectors attached to the vortex indicate contributions to the force $-d\mathbf{F}$ extracted from force per unit length, see Eq. (3) and inset (a) of Fig. 3. They are scaled by factor 3 for better visibility. Projections of the view are shown on sides of the box. Red dashed lines denote shape of nucleus (defined as a point where density of protons drops to value 0.005 fm^{-3}). By blue triangles (on XY-plane) trajectory of the vortex up to given time is shown.

The force \mathbf{f}_{VN} in Eq. (1) is given by $-f(r) \sin \alpha \hat{\mathbf{r}}$. The total force is the sum of contributions from all vortex elements $\mathbf{F} = \int_L d\mathbf{F}$. We model $f(r)$ with a Padé approximant with the asymptotic behavior $f(r \rightarrow \infty) \propto r^{-3}$ consistent with hydrodynamic predictions. The parameters of the Padé approximant are determined from a least-squares fit to all simulation data resulting in the force per unit length $f(r)$ characterization of the vortex-nucleus interaction shown in Fig. 3. (The hydrodynamic results and fitting procedure are described in detail in [16].) This simple characterization of the force \mathbf{F} works better at lower densities, which is consistent with the larger nuclear deformations seen at higher densities. Nuclear deformations introduce an orientation dependence to the force that is not captured by the simple model (3).

Conclusions We have performed unconstrained simulations of a quantum vortex dynamics in superfluid neutron medium in the presence of a nucleus using an appropriate time-dependent extension of DFT to superfluid system. We have determined that the vortex-nucleus force is repulsive and increasing in magnitude with density for the densities characteristic of the neutron star crust (0.014 and 0.031 fm^{-3}). The vortex line shape is strongly affected by the interaction at small separations, leading to significant bending and its lengthening, controlled by the size of the nucleus. Moreover, the vortex-nucleus interaction also induces a deformation of the nucleus. These results demonstrate that the vortex-nucleus interaction cannot be described by a function of

their separation alone. To fully characterize the vortex-nucleus interaction we have extracted the force per unit length for various vortex-nucleus configurations. For velocities of any ambient flow in the background smaller than $v_c \sim (1-5) \times 10^{-4}c$ the pinned superfluid can store enough angular momentum to drive the giant glitches seen in pulsars [17].

We are grateful to K. J. Roche and A. Sedrakian for helpful discussions and comments. We thank Witold Rudnicki, Franciszek Rakowski, Maciej Marchwiany and Kajetan Dutka from the Interdisciplinary Centre for Mathematical and Computational Modelling (ICM) of Warsaw University for useful discussions concerning the code optimization. This work was supported by the Polish National Science Center (NCN) under Contracts No. UMO-2013/08/A/ST3/00708. The method used for generating initial states was developed under a grant of Polish NCN under Contracts No. UMO-2014/13/D/ST3/01940. Calculations have been performed: at the OLCF Titan - resources of the Oak Ridge Leadership Computing Facility, which is a DOE Office of Science User Facility supported under Contract DE-AC05-00OR22725; at NERSC Edison - resources of the National Energy Research Scientific computing Center, which is supported by the Office of Science of the U.S. Department of Energy under Contract No. DE-AC02-05CH11231; at HA-PACS (PACS-VIII) system - resources provided by Interdisciplinary Computational Science Program in Center for Computational Sciences,

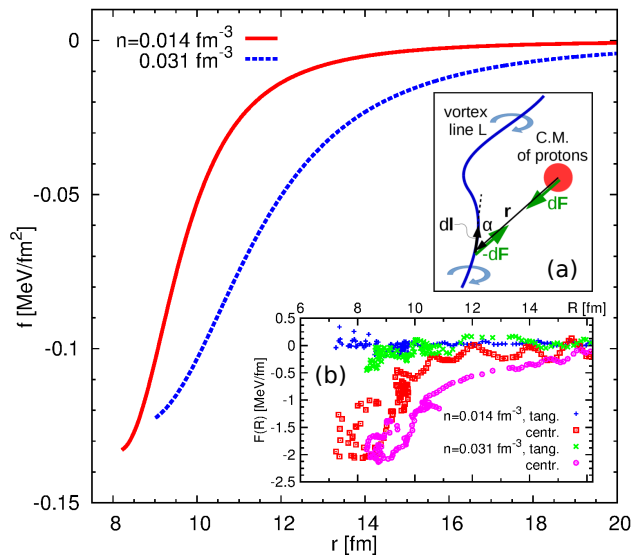


FIG. 3. (Color online) Extracted force per unit length $f(r)$ for both densities. Negative values correspond to the repulsive force. In inset (a) the schematic configuration is shown explaining the extraction procedure according to Eq. (3). Inset (b) shows the measured total force $F(R)$ as shown in Fig. 1 for both densities. The force has been decomposed into tangential and centripetal components with respect to the instantaneous vortex position.

University of Tsukuba. This work was supported in part by U.S. DOE Office of Science Grant DE-FG02-97ER41014, and a WSU New Faculty Seed Grant.

* gabrielw@if.pw.edu.pl
 † sekizawa@if.pw.edu.pl
 ‡ magiersk@if.pw.edu.pl
 § bulgac@uw.edu
 ¶ michael.forbes@wsu.edu

[1] V. Radhakrishnan and R. N. Manchester, Detection of a change of state in the pulsar PSR 0833-45, *Nature* **222**, 228–229 (1969).
 [2] P. E. Reichley and G. S. Downs, Observed decrease in the periods of pulsar PSR 0833-45, *Nature* **222**, 229–230(1969).
 [3] J.M. Lattimer, M. Prakash, The Physics of Neutron Stars, *Science* **304**, 536-542 (2004).
 [4] P.W Anderson, N Itoh, Pulsar glitches and restlessness as a hard superfluidity phenomenon, *Nature* **256**, 25 (1975)
 [5] B. Haskell, A. Melatos, Models of pulsar glitches, *Int. J. Mod. Phys. D* **24**, 1530008 (2015).
 [6] P. M. Pizzochero, L. Viverit, R. A. Broglia, Vortex-nucleus interaction and pinning forces in neutron stars, *Phys. Rev. Lett.* **79**, 3347 (1997).
 [7] P. Donati, P.M. Pizzochero, Is there Nuclear Pinning of Vortices in Superfluid Pulsars, *Phys. Rev. Lett.* **90**, 211101 (2003).

[8] P. Donati, P.M. Pizzochero, Realistic energies for vortex pinning in intermediate-density neutron star matter, *Phys. Lett. B* **640**, 74 (2006).
 [9] P. Donati, P.M. Pizzochero, Fully consistent semiclassical treatment of vortex-nucleus interaction in rotating neutron stars, *Nucl. Phys. A.* **742**, 363 (2004).
 [10] S. Seveso, P. M. Pizzochero, F. Grill and B. Haskell, Mesoscopic pinning forces in neutron star crusts, *MNRAS* **455**, 3952 (2016).
 [11] P. Avogadro, F. Barranco, R. A. Broglia, and E. Vigezzi, Quantum calculation of vortices in the inner crust of neutron stars, *Phys. Rev. C* **75**, 012805(R) (2007).
 [12] P. Avogadro, F. Barranco, R.A. Broglia, E. Vigezzi, Vortex-nucleus interaction in the inner crust of neutron stars, *Nucl. Phys. A* **811**, 378 (2008).
 [13] P. M. Pizzochero, Pinning and Binding Energies for Vortices in Neutron Stars: Comments on Recent Results, (2007), arXiv:0711.3393.
 [14] S. Jin, A. Bulgac, K. Roche, G. Wlazlowski, Coordinate-Space Solver for Superfluid Many-Fermion Systems with Shifted Conjugate Orthogonal Conjugate Gradient Method, (2016), arXiv:1608.03711 [nucl-th].
 [15] A. Bulgac, M.M. Forbes, R. Sharma, Strength of the Vortex-Pinning Interaction from Real-Time Dynamics, *Phys. Rev. Lett.* **110**, 241102 (2013).
 [16] See Supplemental Material at {URL will be provided by the publisher } which includes Refs. [52–60] for discussion of technical aspects including generation of initial configurations, integration of TDSLDA equations, vortex detection algorithm, force per unit length fitting procedure and list of accompanying movies.
 [17] B. Link, Dynamics of Quantum Vorticity in a Random Potential, *Phys. Rev. Lett.* **102**, 131101 (2009).
 [18] *Quantized Vortex Dynamics and Superfluid Turbulence*, Lecture Notes in Physics, Eds. C.F. Barenghi, R.J. Donnelly, W.F. Vinen, Springer-Verlag Berlin Heidelberg 2001.
 [19] R.I. Epstein, G. Baym, Vortex drag and the spin-up time scale for pulsar glitches, *Astrophys. J.* **387**, 276 (1992).
 [20] R.I. Epstein and G. Baym, Vortex pinning in neutron stars, *Ap. J.* **328**, 680 (1988).
 [21] M. Antonelli, P. Pizzochero, Axially symmetric equations for differential pulsar rotation with superfluid entrainment, arXiv:1603.02838 (2016).
 [22] A. Bulgac and S. Yoon, Large Amplitude Dynamics of the Pairing Correlations in a Unitary Fermi Gas, *Phys. Rev. Lett.* **102**, 085302 (2009).
 [23] A. Bulgac, Y.-L. Luo, P. Magierski, K. J. Roche, and Y. Yu, Real-Time Dynamics of Quantized Vortices in a Unitary Fermi Superfluid, *Science*, **332**, 1288 (2011).
 [24] A. Bulgac, P. Magierski, and M.M. Forbes, The Unitary Fermi Gas: From Monte Carlo to Density Functionals, in *BCS-BEC Crossover and the Unitary Fermi Gas*, edited by W. Zwerger, Lecture Notes in Physics, Vol. 836, pp 305-373 (Springer, Heidelberg, 2012).
 [25] A. Bulgac, Y.-L. Luo, and K.J. Roche, Quantum Shock Waves and Domain Walls in Real-Time Dynamics of a Superfluid Unitary Fermi Gas, *Phys. Rev. Lett.* **108**, 150401 (2012).
 [26] A. Bulgac, Time-Dependent Density Functional Theory and Real-Time Dynamics of Fermi Superfluids, *Ann. Rev. Nucl. Part. Sci.* **63**, 97 (2013).
 [27] A. Bulgac, M.M. Forbes, M.M. Kelley, K.J. Roche, and G. Wlazlowski, Quantized Superfluid Vortex Rings in the

- Unitary Fermi Gas, Phys. Rev. Lett. **112**, 025301 (2014).
- [28] G. Wlazłowski, A. Bulgac, M. M. Forbes, and K. J. Roche, Life Cycle of Superfluid Vortices and quantum turbulence in the Unitary Fermi Gas, Phys. Rev. A **91**, 031602(R) (2015).
- [29] I. Stetcu, A. Bulgac, P. Magierski, and K.J. Roche, Isovector Giant Dipole Resonance from 3D Time-Dependent Density Functional Theory for Superfluid Nuclei, Phys. Rev. C **84**, 051309(R) (2011).
- [30] I. Stetcu, C.A. Bertulani, A. Bulgac, P. Magierski, and K.J. Roche, Relativistic Coulomb Excitation within Time-Dependent Superfluid Local Density Approximation, Phys. Rev. Lett. **114**, 012701 (2015).
- [31] A. Bulgac, P. Magierski, K.J. Roche, I. Stetcu, Induced Fission of ^{240}Pu within a Real-Time Microscopic Framework, Phys. Rev. Lett. **116**, 122504 (2016).
- [32] P. Magierski, Nuclear Reactions and Superfluid Time Dependent Density Functional Theory, to appear in *Progress of time-dependent nuclear reaction theory*, Betham Science Publishers 2016.
- [33] J. Negele and D. Vautherin, Neutron star matter at sub-nuclear densities, Nucl. Phys. A **207**, 298 (1973).
- [34] S.A. Fayans, JETP Letters, Towards a universal nuclear density functional, **68**, 169 (1998);
- [35] S.A. Fayans, S.V. Tolokonnikov, E.L. Trykov, D. Zawischa, Nuclear isotope shifts within the local energy-density functional approach, Nucl. Phys. A **676**, 49 (2000)
- [36] B. Friedman and V. R. Pandharipande, Hot and cold nuclear and neutron matter, Nucl. Phys. A **361**, 502 (1981)
- [37] R. B. Wiringa, V. Fiks, and A. Fabrocini, Equation of state for dense nucleon matter, Phys. Rev. C **38**, 1010 (1988).
- [38] Y. Yu and A. Bulgac, Energy Density Functional Approach to Superfluid Nuclei, Phys. Rev. Lett. **90**, 222501 (2003) and *Appendix to: Energy Density Functional Approach to Superfluid Nuclei*, nucl-th/0302007.
- [39] S.V. Tolokonnikov, I.N. Borzov, M. Kortelainen, Yu.S. Lutostansky, and E.E. Saperstein, Fayans functional for deformed nuclei. Uranium region, arXiv:1507.06607, EPJ Web of Conferences, **107**, 02003 (2016), and earlier references therein.
- [40] A. Bulgac and Y. Yu, Spatial Structure of a Vortex in Low Density Neutron Matter, Phys. Rev. Lett. **90**, 161101 (2003).
- [41] A. Bulgac and Y. Yu, Renormalization of the Hartree-Fock-Bogoliubov Equations in the Case of a Zero Range Pairing Interaction, Phys. Rev. Lett. **88**, 042504 (2002).
- [42] A. Bulgac, Local Density Approximation for Systems with Pairing Correlations, Phys. Rev. C **65**, 051305(R) (2002).
- [43] A. Bulgac and Y. Yu, The vortex state in a strongly coupled dilute atomic fermionic superfluid, Phys. Rev. Lett. **91**, 190404 (2003).
- [44] A. Bulgac, Local Density Functional Theory for Superfluid Fermionic Systems: The Unitary Gas, Phys. Rev. A **76**, 040502(R) (2007).
- [45] A. Bulgac and M.M. Forbes, A Unitary Fermi Supersolid: The Larkin-Ovchinnikov Phase, Phys. Rev. Lett. **101**, 215301 (2008).
- [46] A. Sedrakian, Vortex repinning in neutron star crusts, Mon. Not. R. Astron. Soc. **277**, 225 (1995).
- [47] M.J.H. Ku, W. Ji, B. Mukherjee, E. Guardado-Sanchez, L. W. Cheuk, T. Yefsah, and M. W. Zwierlein, Motion of a Solitonic Vortex in the BEC-BCS Crossover, Phys. Rev. Lett. **113**, 065301 (2014).
- [48] M.J.H. Ku, B. Mukherjee, T. Yefsah, and M.W. Zwierlein, Cascade of Solitonic Excitations in a Superfluid Fermi gas: From Planar Solitons to Vortex Rings and Lines, Phys. Rev. Lett. **116**, 045304 (2016).
- [49] N. Andersson, T. Sidery, and G.L. Comer, Superfluid neutron star turbulence, MNRAS **381**, 747 (2007).
- [50] W.F. Vinen, J.J. Niemela, Quantum Turbulence, J. Low Temp. Phys. **128**, 167 (2002).
- [51] M. Tsubota, M. Kobayashi, H. Takeuchi, Quantum hydrodynamics, Phys. Rep. **522**, 191 (2013).
- [52] A. Bulgac, M. M. Forbes, K. J. Roche, and G. Wlazłowski, Quantum Friction: Cooling Quantum Systems with Unitary Time Evolution, (2013), arXiv:1305.6891 [nucl-th].
- [53] R. Takayama, T. Hoshi, T. Sogabe, S.-L. Zhang, T. Fujiwara, Linear Algebraic Calculation of Green's function for Large-Scale Electronic Structure Theory, Phys. Rev. B **73**, 165108 (2006).
- [54] S. Yamamoto, T. Sogabe, T. Hoshi, S.-L. Zhang, T. Fujiwara, Shifted COCG method and its application to double orbital extended Hubbard model, J. Phys. Soc. Jpn. **77**, 114713 (2008).
- [55] S. Gandolfi, A. Gezerlis, and J. Carlson, Neutron matter from low to high density, Annu. Rev. Nucl. Part. Sci. **65**, 303 (2015).
- [56] H. Lamb, Hydrodynamics, Cambridge University Press (1975).
- [57] P. Magierski, A. Bulgac, Nuclear hydrodynamics in the inner crust of neutron stars, Acta Phys. Polon. B35, 1203 (2004).
- [58] P. Magierski, In-medium ion mass renormalization and lattice vibrations in the neutron star crust, Int. J. Mod. Phys. E13, 371 (2004).
- [59] L.G. Cao, U. Lombardo, and P. Schuck, Screening effects in superfluid nuclear and neutron matter within Brueckner theory, Phys. Rev. C **74**, 064301 (2006).
- [60] A.S. Umar, V.E. Oberacker, C.J. Horowitz, P.-G. Reinhard, J.A. Maruhn, Swelling of nuclei embedded in neutron gas and consequences for fusion, Phys. Rev. C **92**, 025808 (2015).

**Supplemental online material for:
“Vortex pinning and dynamics in the neutron
star crust”**

In the supplemental material various technical aspects are discussed related to the generation of initial configurations, integration of TDSLDA equations, and the vortex detection algorithm. We also provide details concerning the fitting procedure, which allows to extract the force per unit length acting on the vortex, and the derivation of the asymptotic expression of the vortex-impurity interaction from irrotational and incompressible hydrodynamics.

INITIAL CONFIGURATIONS

Initial states are prepared as self-consistent solutions of SLDA equations

$$\begin{pmatrix} h & \Delta \\ \Delta^* & -h \end{pmatrix} \begin{pmatrix} u_k \\ v_k \end{pmatrix} = \varepsilon_k \begin{pmatrix} u_k \\ v_k \end{pmatrix}, \quad (4)$$

where the single-particle Hamiltonian h and pairing potential Δ are obtained by taking the appropriate functional derivatives of the energy density functional, and ε_k are single-quasiparticle energies. Standard self-consistent approach requires a series of diagonalizations of the single-quasiparticle Hamiltonian. For the case without the spin-orbit interaction, the Hamiltonian is represented by a matrix of size $(2 \times 50 \times 50 \times 40)^2 = 200,000^2$ (factor 2 corresponds to u and v components of the wave function). Single diagonalization of this matrix (for protons and neutrons) takes about 40 min. on Edison supercomputer (NERSC) [1] with 36,864 cores. Taking into account that more than 100 iterations are required to get a reasonably convergent solution, it gives an unacceptable computational cost of the order of few millions of CPU hours per initial state. For this reason we have used alternative methods to decrease the number of diagonalizations. Namely, we started the process from the uniform matter solution using the real time dynamics (with a desired number of protons and neutrons), and subsequently we slowly turned on the confining potential for neutrons and the harmonic potential for protons. The harmonic potential localizes protons in a desired position in space. The real-time dynamics is supplemented by potential simulating quantum friction (see [2] for details). During this stage quite accurate initial profiles of densities defining the single-quasiparticle Hamiltonian have been created, for a state without vortex. Next, we started self-consistent iterations to compute densities from Green's functions, using the method very similar to the one applied in studies of large electronic systems [3, 4]. The method extracts densities without explicit diagonalization of HFB matrix (for details see [5]). To get a state with a vortex in each iteration we imprinted the correct phase dependence on the neutron pairing potential

Δ . Once the convergence (with a satisfactory accuracy) has been reached we performed a diagonalization in order to extract wave functions. Finally, we performed short real-time dynamics with the quantum friction potential in order to get rid of residual excitations. This methodology allows us to generate an initial states invoking the diagonalization routine only once.

The neutrons are confined in axially symmetric external potential (U_{ext} in MeV, r in fm)

$$U_{\text{ext}}(r) = \begin{cases} 0, & r \leq 30 \\ 50 s(r - 30, 5, 2), & 30 < r < 35 \\ 50, & r \geq 35 \end{cases} \quad (5)$$

where s denotes the switching function,

$$s(x, w, \alpha) = \frac{1}{2} + \frac{1}{2} \tanh \left[\alpha \tan \left(\frac{\pi x}{w} - \frac{\pi}{2} \right) \right]. \quad (6)$$

$r = \sqrt{x^2 + y^2}$ is the distance from the symmetry z -axis. The potential allows to avoid the interference of the quantum vortex with other vortices from neighboring cells. Note that inside the tube the potential is perfectly flat and it does not affect vortex dynamics. Dynamics of a nucleus is also not affected, as long as the nucleus does not touch the boundary.

In order to fit the pairing coupling constant g , we have solved static SLDA equations (4) for uniform neutron matter for various densities. For each density we treated g as a free parameter and we adjusted it to reproduce the value of the neutron pairing gap. The standard BCS theory of superconductivity predicts the density dependence of the pairing gap Δ in pure neutron matter, but overestimates its amplitude (see, e.g., Ref. [6] and references therein). We therefore scale the BCS results to obtain maximum pairing gap of 2 MeV. Note that in our approach both neutrons and protons are superfluid, and that we assume isospin is a good symmetry for the pairing channel (both couplings are equal). In Fig. 4 we present the neutron pairing gap as a function of the Fermi momentum used in the fitting procedure. After tabulating coupling constants g as a function of density n we constructed an interpolating function which has been used subsequently in dynamical simulations.

In Fig. 5 an example of the initial state used in the simulations is shown. Within the box we are able to fit a nucleus and a quantum vortex. It also provides enough space to study the interaction at variety of vortex-nucleus mutual arrangements.

In order to examine the possibilities of both pinning and anti-pinning scenario, we have generated initial states for the background neutron density $n = 0.014 \text{ fm}^{-3}$ and 0.031 fm^{-3} , both for pinned and unpinned configurations. Number of protons is set to be 50, while number of neutrons is about 2,530 and 5,710, respectively. For both densities the energy per particle turned out to be larger for pinned configuration than for

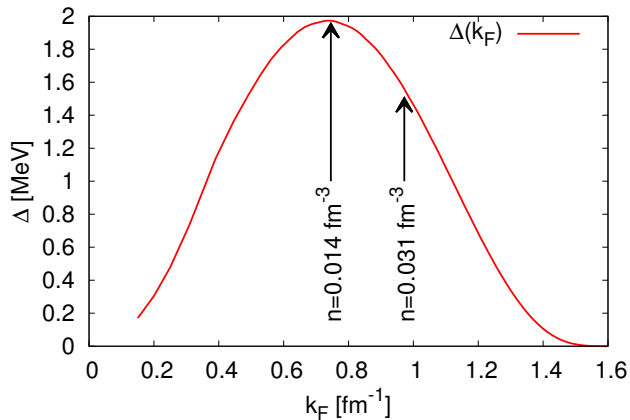


FIG. 4. (Color online) The neutron pairing gap as a function of the Fermi momentum $k_F = (3\pi^2 n)^{1/3}$ used in calculations. Arrows indicate points for which simulations have been performed: $k_F = 0.75 \text{ fm}^{-1}$ and 0.97 fm^{-1} , respectively.

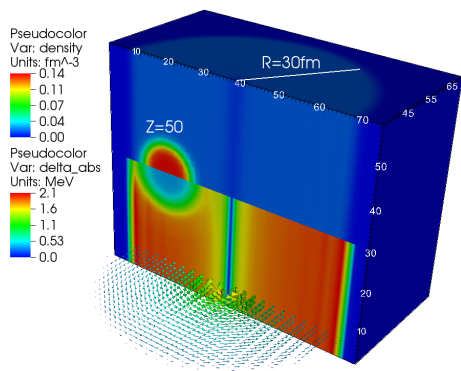


FIG. 5. (Color online) Example of initial unpinned configuration for $n = 0.014 \text{ fm}^{-3}$. The upper part of the box shows the total density distributions, while the lower part shows the absolute value of the neutron pairing potential Δ . The vanishing pairing field and the depletion of the density along the tube symmetry axis are due to the presence of a quantum vortex. Arrows in the bottom part of the figure show the circular flow of neutrons.

the unpinned one. The differences in energy per particle are about 6 keV and 4 keV, respectively for densities $n = 0.014 \text{ fm}^{-3}$ and 0.031 fm^{-3} . A simple estimate of the pinning energy computed as the energy per particle times the average number of particles gives values of 15 MeV and 22 MeV respectively. These numbers are close to values reported in [7] for the SkM* and SGII interactions which have an effective mass close that of the FaNDF⁰ functional we used. We emphasize, however, that these are only estimates. Our initial states are constructed for time-evolution, not for computing energy differences (the pinning energy), and have slightly different numbers of

particles which will introduce additional corrections to the quantitative pinning energy. In Fig. 6 we show the density distribution and the neutron pairing potential for generated initial states.

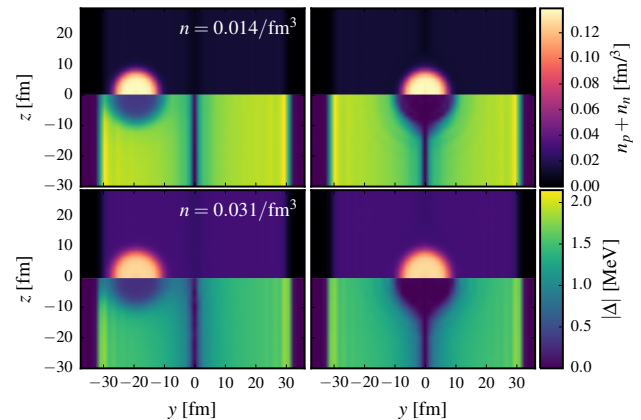


FIG. 6. (Color online) Initial states used for dynamic simulations for neutron background density $n = 0.014 \text{ fm}^{-3}$ (top) and 0.031 fm^{-3} (bottom). In each box the total density distribution (upper half) and the absolute value of the neutron pairing potential (lower half) are shown.

INTEGRATION OF TDSLDA EQUATIONS - TECHNICAL ASPECTS

The TDSLDA equations are formally equivalent to the time-dependent Hartree-Fock-Bogoliubov (TDHFB) in coordinate representation, or time-dependent Bogoliubov-de Gennes (TD BdG) equations

$$i\hbar \frac{\partial}{\partial t} \begin{pmatrix} u_k \\ v_k \end{pmatrix} = \begin{pmatrix} h & \Delta \\ \Delta^* & -h \end{pmatrix} \begin{pmatrix} u_k \\ v_k \end{pmatrix}. \quad (7)$$

We have integrated these equations using the symplectic splitting operator method. The time stepping algorithm consists of the following operations:

$$\begin{pmatrix} u_k(t + \Delta t) \\ v_k(t + \Delta t) \end{pmatrix} = \exp(-i\mathcal{H}\Delta t/\hbar) \begin{pmatrix} u_k(t) \\ v_k(t) \end{pmatrix}, \quad (8)$$

where the matrix $\mathcal{H}(n(t), \nu(t), \dots)$ depends on wavefunctions through densities. The stepping algorithm reaches the highest accuracy if \mathcal{H} is provided for midpoint time $t + \frac{\Delta t}{2}$. We use Heun's method to produce midpoint Hamiltonian, i.e. first we performed a trial step $\varphi_{\text{trial}}(t + \Delta t) = \exp[-i\mathcal{H}(t)\Delta t/\hbar] \varphi(t)$, then from φ_{trial} we computed densities and formed $\mathcal{H}_{\text{trial}}(t + \Delta t)$. Finally we approximated $\mathcal{H}(t + \frac{\Delta t}{2}) \cong \frac{1}{2}[\mathcal{H}(t) + \mathcal{H}_{\text{trial}}(t + \Delta t)]$. In order to perform the operations efficiently, we split Hamiltonian into kinetic and potential parts as $\mathcal{H} = \mathcal{K} + \mathcal{V}$ and apply the Trotter-Suzuki decomposition:

$$e^{-i\frac{\mathcal{H}\Delta t}{\hbar}} = e^{-i\frac{\mathcal{V}\Delta t}{2\hbar}} e^{-i\frac{\mathcal{K}\Delta t}{\hbar}} e^{-i\frac{\mathcal{V}\Delta t}{2\hbar}} + \mathcal{O}(\Delta t^3). \quad (9)$$

Since the effective mass of FaNDF⁰ density functional is density independent, the kinetic part of the Hamiltonian \mathcal{K} is diagonal in momentum representation and the operation $e^{-i\frac{\epsilon\Delta t}{\hbar}}$ can be done efficiently by means of Fourier transforms. The potential part has the following matrix structure,

$$\mathcal{V} = \begin{pmatrix} U(\mathbf{r}) & \Delta(\mathbf{r}) \\ \Delta^*(\mathbf{r}) & -U(\mathbf{r}) \end{pmatrix}, \quad (10)$$

where the submatrices $U(\mathbf{r})$ (mean-field potential) and $\Delta(\mathbf{r})$ (pairing potential) are diagonal in the coordinate representation. The exponent of the potential part can be computed analytically,

$$e^{-i\frac{\mathcal{V}\Delta t}{\hbar}} = \begin{pmatrix} \cos(\frac{\epsilon\Delta t}{2\hbar}) - i\frac{U(\mathbf{r})}{\epsilon} \sin(\frac{\epsilon\Delta t}{2\hbar}) & -i\frac{\Delta(\mathbf{r})}{\epsilon} \sin(\frac{\epsilon\Delta t}{2\hbar}) \\ -i\frac{\Delta^*(\mathbf{r})}{\epsilon} \sin(\frac{\epsilon\Delta t}{2\hbar}) & \cos(\frac{\epsilon\Delta t}{2\hbar}) + i\frac{U(\mathbf{r})}{\epsilon} \sin(\frac{\epsilon\Delta t}{2\hbar}) \end{pmatrix}, \quad (11)$$

where

$$\epsilon = \sqrt{U(\mathbf{r})^2 + |\Delta(\mathbf{r})|^2}. \quad (12)$$

The final complexity of the algorithm is governed by the FFT complexity. Note that this very efficient method cannot be used if spin-orbit term is included ($U(\mathbf{r})$ is no longer diagonal) or the effective mass is density dependent (kinetic part is no longer diagonal in momentum representation).

In the present simulations we have used an integration time step $\Delta t = 0.054$ fm/c. This time step makes the time evolution stable within time intervals of about 18,000 fm/c. Number of evolved wave-functions is about 37,000 for neutrons and 16,000 for protons.

The integration is performed with an external time-dependent potential that couples only to protons,

$$U_{\text{ext}}(\mathbf{r}, t) = -\frac{1}{Z}\mathbf{F}_{\text{ext}}(t) \cdot \mathbf{r}, \quad (13)$$

where Z is the number of protons. According to the Ehrenfest's theorem, this external potential corresponds to an external force,

$$\frac{d\langle\hat{\mathbf{p}}\rangle}{dt} = -\langle\nabla U_{\text{ext}}(\mathbf{r}, t)\rangle = \mathbf{F}_{\text{ext}}(t), \quad (14)$$

which is constant in space. The force is dynamically adjusted during the time evolution in such a way that the resulting motion of protons occurs at a constant velocity.

VORTEX DETECTION

In order to extract the vortex core location, we have analyzed the pairing field Δ . Both the absolute value and the phase of the pairing field has been taken into account.

It is known that in the vortex core the pairing field vanishes, while its phase rotates around this singular point. In our case, it is difficult to obtain precise information on the vortex core position from the location where $|\Delta|$ vanishes, especially in the case of the vortex being close to the nucleus. Because of high neutron density inside the nucleus, the absolute value of pairing gap is very small in this region. Therefore it is difficult to numerically locate the vortex core inside the nucleus only by analyzing the behavior of the pairing gap magnitude. The procedure has to be supplemented by analysis of the pairing phase which allows to identify the vortex core position unambiguously. We found that the phase is weakly affected by the presence of the nucleus, as shown in Fig. 7.

Thus, for each XY-plane we searched for a point around which the phase rotates by 2π and we attributed it to the vortex core position. Next, we created a line connecting vortex cores in each XY-plane using spline interpolation. The vortex core position for XY-plane crossing the center of mass of protons has been used to define the vortex-nucleus distance R .

VORTEX TENSION

The time-dependent simulations allow for estimation of the vortex tension T originating from the quantized

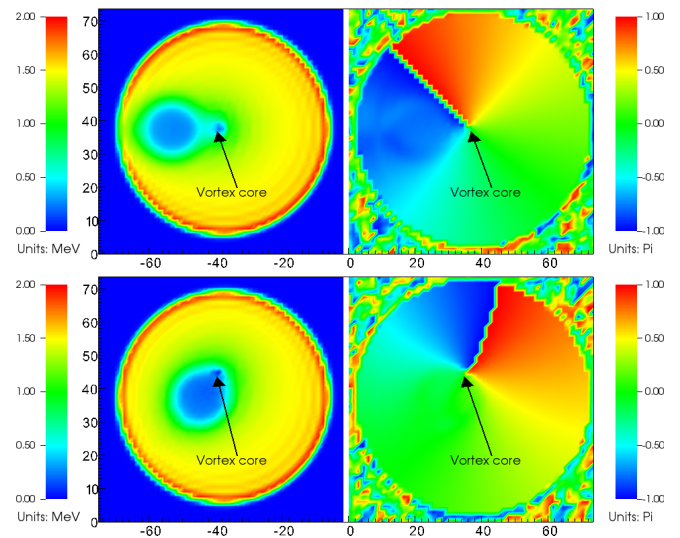


FIG. 7. (Color online) Sections along XY-plane at $z = 30$ fm showing absolute values (left column) and phase (right column) of the pairing potential for two different vortex-nucleus configurations for background neutron density, $n = 0.031$ fm⁻³. Strong suppression of absolute value of the pairing potential is due to presence of the quantum vortex core and the nucleus. The phase of the pairing potential is almost unaffected by the presence of the nucleus, and it can be a clear signal of the vortex core position. Arrow shows detected vortex core position from analysis of the phase.

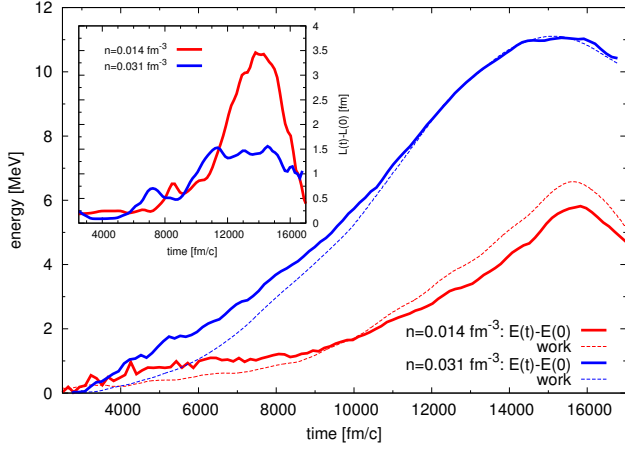


FIG. 8. (Color online) Excitation energy $E(t) - E(0)$ of the system as a function of time. By dashed line work performed by external force computed by formula $W(t) = \int_0^t \mathbf{F}_{\text{ext}}(t') \cdot \mathbf{v}(t') dt'$ is presented. In inset change of vortex length $L(t) - L(0)$ is shown as function of time.

superflow around the core. We have evaluated the excitation energy of the system $E^*(t) = E(t) - E(0)$ as a function of time due to the motion of the impurity. It is related to work performed by the external force $\mathbf{F}_{\text{ext}}(t)$. In Fig. 8 we present $E^*(t)$ and compare it with the work computed according to the formula $W(t) = \int_0^t \mathbf{F}_{\text{ext}}(t') \cdot \mathbf{v}(t') dt'$, where $\mathbf{v}(t)$ is the velocity of the center of mass of the protons. Indeed these two quantities agree with reasonable accuracy. The energy reaches maximum at the configuration corresponding to the vortex having the largest length, see inset of Fig. 8. If we assume that the total excitation energy is absorbed by the vortex, we can estimate the vortex tension as $T \simeq E^*(t_{\text{max}})/\Delta L_{\text{max}}$, where t_{max} corresponds to the time when the vortex achieves the maximum length $L_{\text{max}} = L(0) + \Delta L_{\text{max}}$. Consequently we have extracted values $T \approx 5/3.5 = 1.4$ MeV/fm and $T \approx 11/1.5 = 7.3$ MeV/fm for densities $n = 0.014$ fm $^{-3}$ and 0.031 fm $^{-3}$, respectively. The results admit that the vortex is much stiffer for higher density case. Note that our estimation should be treated as an upper limit for the tension as some fraction of the excitation energy is absorbed by other degrees of freedom related for example to the nucleus, giving rise to the shape deformation. On the other hand such a quantity is more useful than the bare tension, as it takes into account other degrees of freedom whose change may not be easy to disentangle in simplified models describing the vortices in the presence of nuclear impurities.

VORTEX-IMPURITY INTERACTION FROM IRROTATIONAL AND INCOMPRESSIBLE HYDRODYNAMICS

The vortex impurity interaction can be extracted from irrotational and incompressible hydrodynamics following Refs. [8–11]. Within this simplified picture the interaction originates from the distortion of the motion of the superfluid component induced by the presence of the impurity. Using the method of images one can construct a series of corrections to the velocity field. The convergence of the series depends on the ratio between the radius of the impurity and the vortex-impurity distance, which play the role of the expansion parameter. If the ratio is sufficiently small one may extract the leading effect, taking into account the first term of the series only. Namely, let us assume that the vortex is located at $x = y = 0$ along the z axis. Consequently its velocity potential reads: $\frac{\kappa}{2\pi}\phi$, where $\kappa = \oint \mathbf{v} \cdot d\mathbf{r} = 2\pi\hbar/2m_n$ corresponds to the circulation, while ϕ is the angle in XY-plane. The impurity of radius R is located at the distance s along x axis (see Fig. 9). The impurity is defined as having a superfluid density inside denoted by ρ_{in} . In addition the impurity may have an instantaneous arbitrary velocity \mathbf{u} . The presence of the impurity modifies the velocity potential:

$$\Phi_{out}(r, \phi) = \frac{\kappa}{2\pi}\phi + A \frac{(\mathbf{r} - \mathbf{s}) \cdot (\frac{\kappa}{2\pi s} \mathbf{e}_y - \mathbf{u})}{|\mathbf{r} - \mathbf{s}|^3}, \quad (15)$$

where \mathbf{e}_y is the unit vector along the y axis, and A is a constant. The term proportional to A represents the leading correction associated with the presence of the impurity, as it is of the same order $1/s$ at the impurity boundary as the first term. The next order term which would represent the correction due to the presence of the vortex is of the order $1/s^2$ and is neglected here. This velocity potential should match the velocity potential inside the impurity:

$$\Phi_{in}(r, \phi) = B_0 + B_1(\mathbf{r} - \mathbf{s}) \cdot \frac{\kappa}{2\pi s} \mathbf{e}_y + B_2(\mathbf{r} - \mathbf{s}) \cdot \mathbf{u}, \quad (16)$$

where B_i are constants which can be determined from the boundary conditions at the surface of the impurity:

$$\Phi_{in}|_R = \Phi_{out}|_R, \quad (17)$$

$$\rho_{in} \left(\frac{\partial \Phi_{in}}{\partial r} - \mathbf{u} \right) |_R = \rho_{out} \left(\frac{\partial \Phi_{out}}{\partial r} - \mathbf{u} \right) |_R, \quad (18)$$

where the second equation is simply the continuity equation at the surface of the impurity. The above conditions lead to the following expression for the velocity field Φ_{in} :

$$\Phi_{in}(r, \phi) = \left(1 + \frac{A}{R^3}\right) (\mathbf{r} - \mathbf{s}) \cdot \frac{\kappa}{2\pi s} \mathbf{e}_y + \frac{A}{R^3} (\mathbf{r} - \mathbf{s}) \cdot \mathbf{u}, \quad (19)$$

Consequently the total energy of the system reads:

$$E = \frac{1}{2} \rho_{in} \int_{V_i} (\nabla \Phi_{in})^2 d^3r + \frac{1}{2} \rho_{out} \int_{V - V_i - V_{vor}} (\nabla \Phi_{out})^2 d^3r, \quad (20)$$

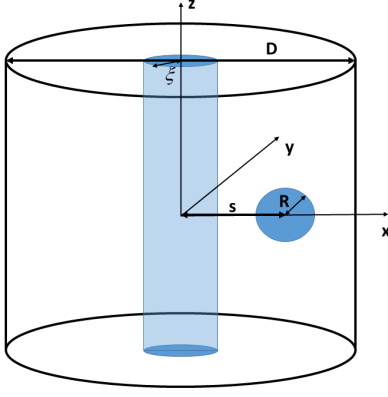


FIG. 9. (Color online) Schematic picture showing the mutual arrangement of the vortex (of radius ξ) and the impurity (of radius R) together with a cylinder of diameter D ($D \rightarrow \infty$) defining the boundary of the system.

where V_i and V_{vor} represent the volumes of the impurity and the vortex, respectively. The volume V denotes the volume of the cylinder shown in the Fig. 9.

The straightforward although lengthy calculations give the following expression for the total energy:

$$E = \frac{1}{4\pi} \rho_{out} \kappa^2 H \ln \left(\frac{D}{2\xi} \right) + \frac{1}{2} \left(\frac{4\pi}{3} R^3 \frac{(\rho_{out} - \rho_{in})^2}{2\rho_{out} + \rho_{in}} \right) u^2 + \left(2\pi R^3 \frac{\rho_{out}(\rho_{in} - \rho_{out})}{2\rho_{out} + \rho_{in}} \right) \left(\frac{\kappa}{2\pi s} \right)^2, \quad (21)$$

where H is the height of the cylinder ($V = \pi D^2 H/4$). The first term represents the logarithmically divergent contribution of the vortex to the energy, the second term corresponds to the kinetic energy of the impurity, whereas the third term is the leading order contribution to the vortex-impurity interaction (neglecting terms $1/s^3$ and higher). Note that the effective mass agrees with the result in Ref. [11]. The obtained result indicates that the force between the vortex and impurity is attractive if $\rho_{in} < \rho_{out}$ and repulsive if $\rho_{in} > \rho_{out}$, and its leading component behaves like $1/s^3$ as a function of the distance. This result requires a comment. In the case when $\rho_{in} = 0$ it has been derived in Ref. [9] providing an argument for the existence of the pinning force. However more general treatment indicates that the anti-pinning effect can appear as well. It is difficult to relate superfluid densities ρ_{in} and ρ_{out} to the densities originating from the microscopic description provided by DFT. Therefore this result should be treated as providing only an asymptotic expression (when $R/s \rightarrow 0$) for the real vortex-impurity interaction, and the sign as well as the magnitude of the coefficient, responsible for the intensity of the force, has to be determined from the microscopic approach. Our parametrization of the pairing interaction underestimates a little the strength of the pairing gaps inside nuclei (where both protons and neutrons

are present) as inferred from phenomenological studies. However, the magnitude of the pairing gap is still a matter of debate [6, 12], and especially for the case of a nucleus embedded in neutron matter it is completely unknown. Nuclei embedded in a neutron superfluid swell, and thus their pairing properties would tend to be more similar to neutron matter [13]. Since we possibly underestimate the pairing gaps inside nuclei, the neutron superfluid fraction is only underestimated in the worst case, if one were to use the hydrodynamic calculation (21). Therefore the repulsive force between the vortex and the nucleus is underestimated as well. The previous hydrodynamic calculation of the vortex-nucleus interaction [9] assumed that $\rho_{in} \equiv 0$, which resulted in an attractive force, not repulsive as we obtain. The character of the pairing in a nucleus immersed in neutron superfluid is not known from ab initio calculations

The first term in Eq. (21) represents the energy of the vortex E_{vor} inside the cylinder and can be used to calculate the vortex tension $T = \frac{dE_{vor}}{dH}$ characterizing the stiffness of the vortex. The formula allows to determine the vortex tension as a function of superfluid (neutron matter) density ρ_s . Namely: $T = \frac{1}{4\pi} \rho_s \kappa^2 \ln \frac{D}{2\xi}$, where D is the diameter of the Wigner-Seitz cell and the size of the vortex core ξ is related to the coherence length [14].

FORCE PER UNIT LENGTH - FITTING DETAILS

In order to extract the force per unit length $f(r; \{a_k, b_k\})$ we minimized weighted χ^2 quantity of the form,

$$\chi_w^2 = \sum_{i=1}^N w(|\mathbf{F}_i|) \left(\mathbf{F}_i - \mathbf{F}_i^{(f)}(\{a_k, b_k\}) \right)^2, \quad (22)$$

with respect to parameters $\{a_k, b_k\}$, where i counts set of measurements (frames from movies), \mathbf{F}_i is measured total force for each measurement, and $\mathbf{F}_i^{(f)}$ is the predicted total force,

$$\mathbf{F}_i^{(f)} = \int_{L_i} f(r; \{a_k, b_k\}) \sin \alpha \mathbf{e}_r dl. \quad (23)$$

(See the main text for meaning of symbols in the above equation). To parametrize $f(r)$ we have used Padé approximant

$$f(r) = \frac{\sum_{k=0}^n a_k r^k}{1 + \sum_{k=1}^{n+3} b_k r^k}, \quad (24)$$

where we imposed asymptotic behavior $f(r \rightarrow \infty) \propto 1/r^3$, predicted by irrotational, incompressible hydrodynamics. Number of fitting parameters is $2n + 4$. Our set of measurements contain mostly configurations with

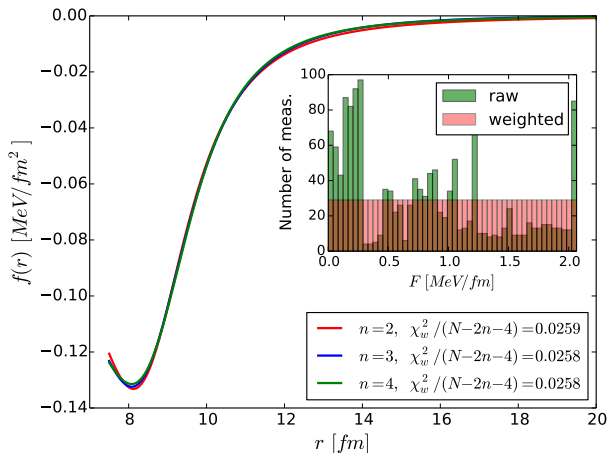


FIG. 10. (Color online) Force per unit length for different orders of Padé approximant for density 0.014 fm^{-3} . Weighted χ^2 per degree of freedom saturates at order $n = 2$. In inset (raw) histogram of measured forces $|\mathbf{F}_i|$ is shown. After introducing weights the histogram becomes uniform.

significant separations R , where the vortex-nucleus interaction is weak. To prevent these measurements to dominate χ^2 we introduced weights $w(|\mathbf{F}_i|)$, in such a way to get the uniformly weighted histogram of measured forces $|\mathbf{F}_i|$, see inset of Fig. 10. We have checked the influence of the weighting form w on the final result and we found that this dependence is very weak.

We have performed minimization for different orders of Padé approximants and we found that negligible improvements of χ_w^2 are gained for orders higher than $n = 2$. Weighted chi-square per degree of freedom saturates at values $\chi_w^2/(N - 2n - 4) \cong 0.026$ and 0.038 for densities 0.014 fm^{-3} and 0.031 fm^{-3} respectively. The corresponding unweighted (all $w(|\mathbf{F}_i|) = 1$) values are $\chi_{w=1}^2/(N - 2n - 4) \cong 0.025$ and 0.054 . In Fig. 10 we demonstrate the convergence of Padé approximant for different orders ($n = 2, 3, 4$) for lower density case. From the figure, good convergence of the Padé approximant can be seen. The fit is meaningful only for $r \gtrsim 8 \text{ fm}$ and $r \gtrsim 9 \text{ fm}$ for densities $n = 0.014 \text{ fm}^{-3}$ and $n = 0.031 \text{ fm}^{-3}$, respectively, and thus, the appearing minimum of the force per unit length for small separations has no meaning. In Table I we provide values of coefficients a_k and b_k for $n = 2$. To show the quality of reproduction of the total force, we have shown in Fig. 11 the measured force \mathbf{F}_i (blue solid line) and the reconstructed force $\mathbf{F}_i^{(f)}$, according to Eq. (23) with Padé approximants $n = 2$ as a function of time. Top (bottom) panel shows results for background neutron density, $n = 0.014 \text{ fm}^{-3}$ (0.031 fm^{-3}).

In order to quantify goodness of the fit one should con-

sider reduced chi-squared statistic

$$\chi_{\text{red.}}^2 = \frac{1}{N - 2n - 4} \sum_{i=1}^N \frac{(\mathbf{F}_i - \mathbf{F}_i^{(f)})^2}{\sigma_i^2}, \quad (25)$$

where σ_i is uncertainty of i -th measurement. Fit is considered as meaningful if $\chi_{\text{red.}}^2 \approx 1$. Oscillations of the measured force seen in Fig. 11 clearly demonstrate that the measurements are affected by uncertainties. (Their source is discussed in next section.) They are of size $0.2 - 0.3 \text{ MeV/fm}$ and it can be used as estimate of the measurement uncertainty σ . Then we can estimate the reduced statistics

$$\chi_{\text{red.}}^2 \cong \frac{1}{N - 2n - 4} \frac{\chi_{w=1}^2}{\sigma^2}. \quad (26)$$

For both densities we obtain value close to one. It confirms that the fit is meaningful at statistical level.

VELOCITY OF THE NUCLEUS

The measured force \mathbf{F}_i shown in Fig. 11 exhibits noticeable fluctuations with a period as large as $2,000 \text{ fm}/c$. In order to check the origin of the fluctuations, we have performed the following simulation: starting from the state where nucleus ($Z = 50$) is immersed in a neutron superfluid ($n = 0.014 \text{ fm}^{-3}$) without vortex, we accelerated the nucleus along z axis up to $v = 0.001 c$. Then, we switched off the external potential. In Fig. 12, the velocity of center of mass of protons is shown as a function of time. In the ideal situation where no energy transfer to internal degrees of freedom is present, the velocity should stay constant. Indeed, as shown in Fig. 12, we observed the nuclear motion with a roughly constant velocity. However, we found that the velocity is also fluctuating about the value $v = 0.001 c$ with a similar period as that observed in the measured force shown in Fig. 11. We concluded therefore that the fluctuations are due to excitations of a background neutron superfluid induced by the motion of the nucleus. We expect that the fluctuations will disappear in the limit of $v \rightarrow 0$. We would

| | $n = 0.014 \text{ fm}^{-3}$ | $n = 0.031 \text{ fm}^{-3}$ |
|--------------------------------|-----------------------------|-----------------------------|
| a_0 [MeV fm ⁻²] | -4549.83 | -3735.28 |
| a_1 [MeV fm ⁻³] | -4525.79 | -988.42 |
| a_2 [MeV fm ⁻⁴] | -505.60 | -4257.99 |
| b_1 [fm ⁻¹] | 6455.46 | 6738.74 |
| b_2 [fm ⁻²] | 6299.41 | 8430.92 |
| b_3 [fm ⁻³] | 23440.34 | 35498.57 |
| b_4 [fm ⁻⁴] | -5640.24 | -7190.64 |
| b_5 [fm ⁻⁵] | 341.73 | 397.51 |

TABLE I. Coefficients of Padé approximant for $n = 2$.

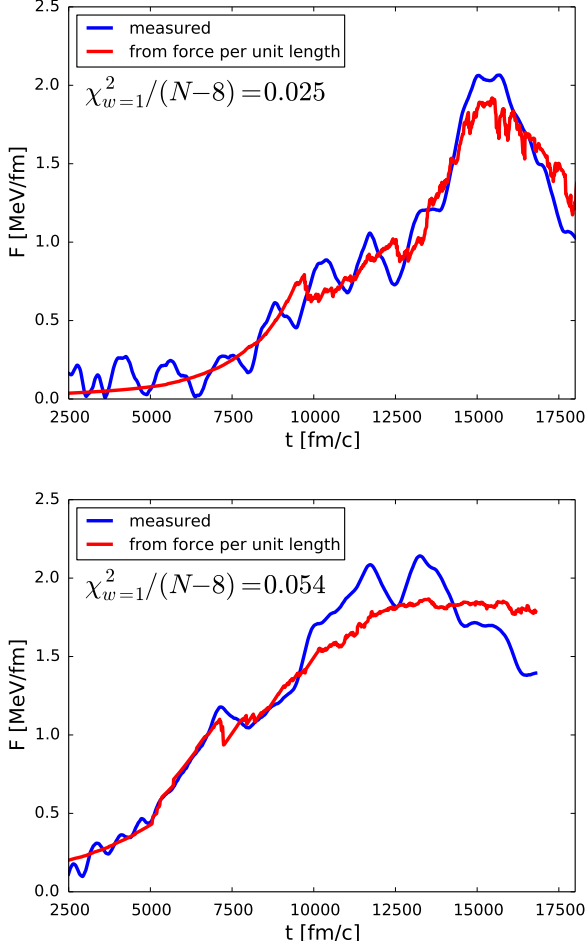


FIG. 11. (Color online) Quality of the total force $|F|$ reproduction as a function of time for $n = 0.014 \text{ fm}^{-3}$ (top) and $n = 0.031 \text{ fm}^{-3}$ (bottom). Value of unweighted chi-square per degree of freedom is also given.

like to emphasize that the conclusions of this paper are not affected by the fluctuations.

We note that the dragging velocity $v = 0.001 c$ is far below the critical velocity of the system and is sufficiently small that the systems follow an almost adiabatic path: for example, after dragging the nucleus for a time of 17,000 fm/c, we increased the energy per particle by less than 0.2 keV.

MOVIES

We provide movies showing dynamics of the system. Elements shown in the movies are:

Red dot: Position of the center of mass of protons.

Blue line: Position of the quantum vortex core.

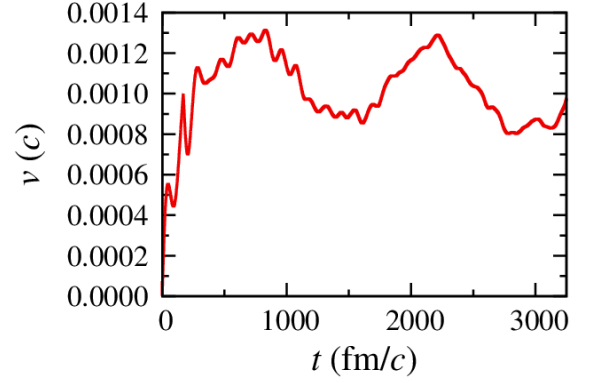


FIG. 12. (Color online) Velocity of center of mass of protons as a function of time for a state with $n = 0.014 \text{ fm}^{-3}$ without vortex. See text for details.

Black vector attached to Red dot: Measured vortex-nucleus force F .

Green vector attached to Red dot: Reconstructed vortex-nucleus force from extracted force per unit length.

Green vectors attached to Blue line:

Contributions to the reconstructed force generated by each vortex element. They are plotted with minus sign and multiplied by factor 3 for better visibility.

Dashed red line: Shape of the nucleus defined as points where density of protons drops to value 0.005 fm^{-3} .

Blue triangles on XY-plane: Trajectory of central element of the vortex up to given time is shown.

Label $F_m(R)$: Absolute value of the measured force for a given frame. In parenthesis distance R between the center of mass of protons and the quantum vortex (as defined in section *Vortex detection*) are shown.

Label $F_r(R)$: Absolute value of the force computed from the extracted force per unit length.

Label Q : Quadrupole moment of proton density distribution.

For better visibility projections of main view along frame axes are depicted on sides of the box.

List of movies:

1. File: `n0_014_unpinned.mp4`
Dynamics of the system with background neutron density $n = 0.014 \text{ fm}^{-3}$ and a nucleus consisting of 50 protons. Initial state: unpinned configuration (top left panel of Fig. 6). Algorithm for the external force adjustment needs about 2,500 fm/c to

put the nucleus into constant velocity movement. Only after this time, the force can be attributed as vortex-nucleus force.

YouTube: <https://youtu.be/yIS3I36wQ9U>

2. File: `n0_031_unpinned.mp4`

Dynamics of the system with background neutron density $n = 0.031 \text{ fm}^{-3}$ and a nucleus consisting of 50 protons. Initial state: unpinned configuration (bottom left panel of Fig. 6).

YouTube: <https://youtu.be/rFP7Tbh1mVQ>

3. File: `n0_014_pinned.mp4`

Dynamics of the system with background neutron density $n = 0.014 \text{ fm}^{-3}$ and a nucleus consisting of 50 protons. Initial state: pinned configuration (top right panel of Fig. 6). The force is not shown as our algorithm for the external force adjustment needs about 2,500 fm/c to put the nucleus into constant velocity movement, and obtained force is not vortex-nucleus force.

YouTube: <https://youtu.be/qdQHj4wjkv8>

4. File: `n0_031_pinned.mp4`

Dynamics of the system with background neutron density $n = 0.031 \text{ fm}^{-3}$ and a nucleus consisting of 50 protons. Initial state: pinned configuration (bottom right panel of Fig. 6).

YouTube: <https://youtu.be/DRRNJey-1Bg>

5. File: `n0_014_unpinned_with_f.mp4`

Movie demonstrating quality of the total force reconstruction by the force per unit length for simulation `n0_014_unpinned.mp4`.

YouTube: <https://youtu.be/Eb459PyyS4A>

6. File: `n0_031_unpinned_with_f.mp4`

Movie demonstrating quality of the total force reconstruction by the force per unit length for simulation `n0_031_unpinned.mp4`.

YouTube: <https://youtu.be/av1k4vZuGrM>

In addition, we provide a movie showing response of spinning gyroscope when pushed. It demonstrates that rotating object moves perpendicular to the external force and direction of the response is set by $\mathbf{\Omega} \times \mathbf{F}$, where $\mathbf{\Omega}$ is angular velocity and \mathbf{F} is external force.

File: `gyroscope.mp4`

YouTube: <https://youtu.be/iYLjmC7fpzk>

* gabrielw@if.pw.edu.pl

† sekizawa@if.pw.edu.pl

‡ magiersk@if.pw.edu.pl

§ bulgac@uw.edu

¶ michael.forbes@wsu.edu

[1] www.nersc.gov/systems/edison-cray-xc30/

[2] A. Bulgac, M. M. Forbes, K. J. Roche, and G. Wlazłowski, Quantum Friction: Cooling Quantum Systems with Unitary Time Evolution, (2013), arXiv:1305.6891 [nucl-th]

[3] R. Takayama, T. Hoshi, T. Sogabe, S.-L. Zhang, T. Fujiwara, Linear Algebraic Calculation of Green's function for Large-Scale Electronic Structure Theory, Phys. Rev. B **73**, 165108 (2006).

[4] S. Yamamoto, T. Sogabe, T. Hoshi, S.-L. Zhang, T. Fujiwara, Shifted COCG method and its application to double orbital extended Hubbard model, J. Phys. Soc. Jpn. **77**, 114713 (2008).

[5] S. Jin, A. Bulgac, K. Roche, G. Wlazłowski, Coordinate-Space Solver for Superfluid Many-Fermion Systems with Shifted Conjugate Orthogonal Conjugate Gradient Method, (2016), arXiv:1608.03711 [nucl-th].

[6] S. Gandolfi, A. Gezerlis, and J. Carlson, Neutron matter from low to high density, Annu. Rev. Nucl. Part. Sci. **65**, 303 (2015).

[7] P. Avogadro, F. Barranco, R.A. Broglia, E. Vigezzi, Vortex-nucleus interaction in the inner crust of neutron stars, Nucl. Phys. A **811**, 378 (2008).

[8] H. Lamb, Hydrodynamics, Cambridge University Press (1975).

[9] R.I. Epstein and G. Baym, Vortex pinning in neutron stars, Ap. J. **328**, 680 (1988).

[10] P. Magierski, A. Bulgac, Nuclear hydrodynamics in the inner crust of neutron stars, Acta Phys. Polon. B35, 1203 (2004).

[11] P. Magierski, In-medium ion mass renormalization and lattice vibrations in the neutron star crust, Int. J. Mod. Phys. E13, 371 (2004).

[12] L.G. Cao, U. Lombardo, and P. Schuck, Screening effects in superfluid nuclear and neutron matter within Brueckner theory, Phys. Rev. C **74**, 064301 (2006).

[13] A.S. Umar, V.E. Oberacker, C.J. Horowitz, P.-G. Reinhard, J.A. Maruhn, Swelling of nuclei embedded in neutron gas and consequences for fusion, Phys. Rev. C **92**, 025808 (2015).

[14] S. Seveso, P. M. Pizzochero, F. Grill and B. Haskell, Mesoscopic pinning forces in neutron star crusts, MNRAS **455**, 3952 (2016).